Journal of Materials Chemistry C

Emission spectrum and strain-dependent properties of inkjet printed heterostructure WSe2-graphene flexible photodetectors

Journal:	*Journal of Materials Chemistry C*
Manuscript ID	TC-ART-10-2023-003741.R1
Article Type:	Paper
Date Submitted by the Author:	31-Mar-2024
Complete List of Authors:	Hossain, Ridwan; University of North Texas, Materials Science and Engineering Bandyopadhyay, Avra; University of North Texas, Electrical Engineering Adhikari, Nirmal; University of North Texas, Materials Science and Engineering Aryal, Sujan; University of North Texas, Materials Science and Engineering Kaul, Anupama; University of North Texas, Materials Science and Engineering; University of North Texas, Electrical Engineering

Emission spectrum and strain-dependent properties of inkjet printed heterostructure WSe_2-graphene flexible photodetectors

Ridwan F. Hossain[†+], *Avra S. Bandyopadhyay*[†+], *Nirmal Adhikari*[†], *Sujan Aryal,*[†] *and Anupama B. Kaul*[†‡*]

[†]Department of Electrical Engineering, [‡]Department of Materials Science and Engineering, University of North Texas, Denton, TX 76203, USA

*Corresponding Author Email: anupama.kaul@unt.edu

[+]These authors contributed equally to the work

Abstract

Heterostructures of WSe_2, a two-dimensional (2D) layered material, offer exciting opportunities for optoelectronics and sensors, including in flexible, conformal modalities. In this work, few layer WSe_2 was synthesized via liquid-phase exfoliation (LPE) where an all inkjet printed WSe_2-graphene heterostructure photodetector was assembled on flexible polyimide substrates and its optoelectronic transport properties characterized. Molecular vibrational spectra were gathered using Raman Spectroscopy as a function of temperature from 80 K to 573 K for the few-layer LPE processed WSe_2 membranes, from which we infer behaviors related to electron-phonon interactions and phonon lifetimes. The Raman-active E^1_{2g} and A_{1g} modes experienced a red-shift as temperature was raised, attributed to the lattice potential anharmonicity. The subsequent integration of the LPE-synthesized WSe_2 into photodetectors led to the validation of photoresponse toward incoming broadband white-light radiation, where the capacitance-frequency response was also measured. Here, the photoresponsivity was calculated to be ~ 0.70 A/W, and other parameters such as detectivity and linear dynamic range were also deduced. Temporal measurements revealed the rise and decay times of the photocurrent with respect to the power density, where the rising and falling edge time constants were within the hundred millisecond range. Strain-dependent measurements conducted with bending showed the photocurrent to decrease with increasing bending and strain, as expected. Finally, strain-dependent Raman measurements revealed a blue-shift and increase in emission intensity for both the in-plane and out-of-plane vibrational modes. Our results indicate the promise of heterostructure WSe_2 devices for large format photoabsorbers printed on flexible substrates using additive manufacturing approaches, where such devices will be attractive for light-weight wearable and airborne applications.

Keywords: 2D materials, WSe_2, solution exfoliation, optoelectronics, flexible electronics, strain-dependent properties, Raman Spectroscopy

1. Introduction

Tungsten di-selenide (WSe_2), a two-dimensional (2D) semiconducting van der Waals solid [1] with a bandgap that lies in the visible region from 1.2 eV to 1.6 eV [2][3][4], is gaining increased attention for optoelectronics given the strong interaction it has with incoming light. The exploration of WSe_2 revealed it's unique features, such as a layer-dependent tunable bandgap [5], direct-to-indirect bandgap crossover [5], photo-switching [6], gate tunable superconductivity and excellent electrostatic coupling [7], to name a few of its exciting properties. Most transition metal dichalcogenide (TMDC) materials, such as MoS_2, $MoSe_2$, and WS_2 are *n*-type semiconductors, but WSe_2 has shown to exhibit a *p*-type character [8], that is, conduction via holes [9] including with palladium electrodes [10]. The *p-n* heterojunction formed by stacking WSe_2 and other TMDCs contribute to improving photoelectric performance [11] towards novel device designs and architectures. Moreover, conventional heterostructures are mainly based on group IV, III-V, or II-VI semiconductors with covalent bonding between atoms at the heterojunctions. Hence, the resulting atomic-scale interface roughness and composition variation at the heterointerface, induced from atomic interdiffusion during growth, inevitably compromises the performance of the devices formed with such heterostructures. In TMDCs however, individual layers are weakly bonded through the van der Waals interaction where the presence of surface dangling bonds [1-4] is minimal upon exfoliating such membranes from their parent bulk crystallites. The absence of dangling bonds even within exfoliated membranes helps ensure more pristine 2D heterointerfaces. This feature in 2D materials broadly, and more specifically in inks formed from 2D materials, makes it feasible to realize structures such as graphene-MoS_2, MoS_2-WSe_2 stacked junctions easily at low temperatures, which is useful for the realization of novel flexible electronic, optoelectronic and sensing devices.

Although confinement effects in the electronic and excitonic dispersion relation in atomically thin sheets of WSe_2 have been extensively studied to date [12][13], the phonon behavior and its modulation with temperature and strain has received less attention. The vibrational properties emerging from phonon-phonon and electron-phonon interactions has a significant influence on the electronic and optoelectronic transport properties of WSe_2 and the ensuing device performance. Raman and photoluminescence spectroscopies have played a major role in elucidating the structural, optical, and mechanical properties of layered TMDCs, including for monolayer or few layer WSe_2 [14][15]. Heat dissipation mechanisms and thermal conductivity play an influential role in determining the eventual device performance, and such properties can, to some extent, be deciphered via Raman peak position and intensity shifts as a function of temperature *T*. In this study, the vibrational properties of few-layer WSe_2 were examined from ~ 80 K to 573 K and the *T*-dependent Raman spectra of few layer WSe_2 is discussed to assess some of these properties, such as phonon-phonon interactions, by examining the full-width-at-half-maximum (FWHM), phonon lifetime, and strain-dependent characterization of the spectrum.

The aforementioned vibrational spectroscopy analysis was conducted on solution-dispersed WSe_2, where the inks generated from the dispersions were then used to construct flexible heterostructure WSe_2-graphene photoabsorbers. The broad appeal of flexible electronics arises from the ability to construct electronic circuits using low-cost techniques well-established in the inkjet printed electronics industry, which is expected to capture a $49.2 billion-dollar market by 2027 [16]. Inkjet printing with its additive manufacturing approaches uses pico-liter droplets of conductive/semi-conductive ink deposited on a wide variety substrates over large areas [17][18].

The approach offers several advantages, such as: (a) low-cost, non-contact, fast fabrication with minimum potential for contamination; (b) pattern quality of printed features is not, in principle, limited by the depth-of-focus of the optics which lithographically fabricated structures depend upon in a traditional clean-room facility; (c) use of drop-on-demand (DOD) digital fabrication technology without the need for physical masks where material is applied only where it is needed; (d) the ability to print both organic and inorganic materials without losing any device functionality. Surveying the literature over recent years, inkjet printed 2D materials have indeed been a center of attention towards devices on flexible formats, ranging from photodetectors [17], transistors [19], sensors [20], and RF antennas [21], but there is little prior work conducted on inkjet printed WSe_2. Of these few reports, Kelly *et al.* [22] demonstrated all-printed, vertically-stacked transistors with graphene source, drain, and gate electrodes, with WSe_2 as the semiconductor channel material, and boron nitride as a dielectric formed from liquid-exfoliated nanosheet networks. In another study, Patel *et al.* [23] used liquid exfoliated and electrophoretically deposited $MoSe_2/WSe_2$ film that is transparent and continuous and can be employed in a photoelectrochemical system, such as a dye-sensitized solar cell and for the production of hydrogen.

In this work, we report on solution-exfoliated WSe_2 and examining its vibrational properties towards the subsequent use in the construction of inkjet deposited WSe_2-graphene heterostructures

printed on flexible polyimide substrates for photodetector applications. Besides vibrational spectroscopy measurements conducted on our few layer membranes as a function of temperature to gauge anharmonic thermal transport effects studied using Raman spectroscopy, the temperature-dependent and strain-dependent optoelectronic measurements were also performed on the photodetector devices. Lastly, capacitance-frequency measurements were also performed as a function of temperature to comment on the trap states. The analysis provided in this work will help in our understanding of solution-processed WSe_2 which will facilitate the development of high-sensitivity photodetectors based on heterostructures of WSe_2 toward scalable flexible electronics and photonics applications in the future.

2. Results

2.1 Raman and Photoluminescence Spectroscopy

Liquid exfoliated WSe_2 membranes were characterized using Raman spectroscopy to study the electronic and vibrational properties as shown by the typical Raman spectra of a WSe_2 membrane in Figure 1(a), gathered using a 532 nm laser at room temperature. The spectra depict two prominent modes, i.e., the E^1_{2g} appearing at ~ 249.3 cm^{-1} due to the in-plane vibrations, and the A^1_g mode appearing at ~ 256.5 cm^{-1} due to the out-of-plane vibrational modes. The intensity of the A^1_g peak was almost half the intensity of the E^1_{2g} peak, which suggests that the exfoliated WSe_2 membranes are not bulk and approach the few-layer regime.

The bottom left inset displays the WSe_2 flake that was isolated by spin coating the WSe_2 ink on the SiO_2/Si substrate. The spectra of the few layer flake was compared with that of bulk WSe_2, as shown by the data in the top-right inset. From the Raman spectra for few-layer and bulk WSe_2 depicted in Figure 1(a), the blue shift in the Raman peak from bulk (e.g., for E_{2g} at ~ 242 cm^{-1}) to few-layer (e.g., for E_{2g} at ~ 249 cm^{-1}) could be due to the contribution of additives in the ink during

liquid exfoliation which sparsely bind the flakes, and hence the thicker, solution-processed film will be a more porous structure per unit volume. This is compared to a few-layer WSe_2 film which will be more dense per unit volume, with atoms that are more strongly bound in WSe_2, interacting via the covalent interaction, that reflects itself as a blue shift. The denser film with the stronger binding between atoms in the few layer membranes may likely be the reason for the blue shift in the Raman peaks evident in the thinner films. In the bulk WSe_2 flake, the A^1_g peak intensity increased compared to the relative intensity of the E^1_{2g} peak. Our results for peak intensity variations are consistent with that of Tonndorf *et al.* [24] who also observed the A^1_g peak intensity to be higher compared to the E^1_{2g} peak intensity for bulk WSe_2.

Photoluminescence (PL) spectra shown in Figure 1(b) illustrates the multiple emission peaks that broaden slightly and systematically shift to lower energies with increasing thickness. Here, the peaks are labeled as the excitonic *A* and *B* peaks with the energy split from the valence band spin-orbital coupling and represent direct bandgap optical transitions, and the indirect *I* peak referring to the indirect optical transitions. The location of the *A* and *B* peaks are ~ 1.54 eV and ~ 1.97 eV, respectively, while the *I* peak occurs at ~ 1.26 eV, confirming that our liquid exfoliated WSe_2 membranes are few layer [12]. Also, the splitting in energy between the *A* and *B* peaks is in close agreement to prior work [25], which report this to be ~ 420 meV for monolayer to few layer WSe_2. The inset in Figure 1(b) shows the PL of bulk WSe_2 membranes, measured under identical conditions, where the *A* peak red-shifts to ~ 1.25 eV, approaching the indirect *I* peak at ~ 1.21 eV, but the intensity of the former was significantly weaker, consistent with expected results for indirect bandgap transitions [25]. Here, we observe a red-shift in the PL peaks from few layers (e.g., for the excitonic A peak at ~ 1.54 eV) to bulk (e.g., for the excitonic A peak at ~ 1.25 eV), which is likely due to quantum confinement effects, a phenomenon well studied in 2D materials.

The band gaps in thinner membranes of semiconducting 2D layered materials typically increase upon thinning the bulk material due to band alignment occurring from thinner, more quantum confined structures. Figure 1(c) depicts the position of the E^1_{2g} and A_{1g} peaks with temperature T where a red-shift is evident as T increases. The increased phonon-phonon coupling at elevated temperatures, which is often dissipative, is believed to be the origin of this red-shift, while the anharmonic contributions to the interatomic potential energy causes thermal expansion upon exposure to heat, consistent with the behavior of most materials [26].

The first order T-coefficient χ for the E^1_{2g} and A_{1g} modes was determined using the Lorentzian fit as a function of T according to,

$$\omega(T) = \omega_0 + \chi T \quad (1)$$

where ω_0 is the phonon frequency at zero Kelvin. As the T increases, the Raman shift for the E^1_{2g} and A_{1g} modes are ~ 7.3 cm^{-1} (from 252.3 cm^{-1} to 245 cm^{-1}) and 8 cm^{-1} (from 261 cm^{-1} to 253 cm^{-1}), respectively. From the slope of the fit in Figure 1(c), χ for the E^1_{2g} and A_{1g} modes, $\chi_{E^1_{2g}}$ and $\chi_{A_{1g}}$, respectively, were determined to be ~ - 0.018 cm^{-1}/K in both cases, which appears to be in good agreement with prior work [27] [28]. A comparative analysis for $\chi_{E^1_{2g}}$ and $\chi_{A_{1g}}$ with other reported work is shown in Table I. For few-layer, liquid exfoliated MoS_2, the $\chi_{E^1_{2g}}$ and $\chi_{A_{1g}}$ were found to be - 0.014 cm^{-1}/K and - 0.016 cm^{-1}/K, respectively [27]. The T dependence of the Raman-active modes is governed by phonon-phonon coupling which often increases in strength with temperature, often also reducing the electron mobility in the material due to greater scattering [29].

Shown in Figure 2(a) is the A_{1g}/E^1_{2g} intensity ratio as a function of T. Below ~ 150 K, the ratio increases slightly, indicating the phonon active A_{1g} mode is relatively stronger or increasing faster than the E^1_{2g} mode. Figure 2(b) illustrates the change in normalized E^1_{2g} and A_{1g} peak intensities with T. Interestingly, the change in intensity for the E^1_{2g} mode is not as noticeable with T whereas

the A_{1g} peak intensity goes up steadily with increasing T. Figure 2(c) depicts the full-width-at-half-maximum (FWHM) of the E^1_{2g} and A_{1g} modes for few-layer WSe_2, which increases by an amount of ~ 12.9 cm^{-1} (from ~ 6.4 cm^{-1} to 19.3 cm^{-1}) and ~ 4.0 cm^{-1} (from ~ 2.8 cm^{-1} to 6.8 cm^{-1}), respectively. The peak broadening arising from the rise in the FWHM is often used to determine the lifetime of phonons, which we also calculate here from the data shown in Figure 2(d); here phonon lifetime τ is shown as a function of T and is calculated using the energy uncertainty relationship in Eqn. 2,

$$\tau = \frac{\hbar}{\Gamma} \tag{2}$$

where $\hbar = 5.3 \times 10^{-12}$ $cm^{-1}s$ and Γ is the FWHM. The decrease in τ with increasing T is primarily due to the decay of strongly interacting optical phonons into weakly interacting low-energy phonons. With increasing T, more phonon modes are activated, resulting in an increase in their densities and vibrational amplitudes, which in turn decreases τ. Evidently, scattering by crystalline defects inherent within the native material, including from surfaces, can influence τ as well. Our analysis here showed τ for the E^1_{2g} and A_{1g} modes to be ~ 0.57 ps and 0.74 ps, respectively, while other reports calculated a slightly higher τ for both peaks [27][30][31]. Table II provides a comparison of τ at room T, where Khan *et al.* [27] measured τ for few layer solution-exfoliated MoS_2 to be ~ 2.2 ps and ~ 1.8 ps for the E^1_{2g} and A_{1g} modes, respectively, while Ko *et al.*[30] determined these values to be ~ 1.8 and 0.84 ps, respectively for monolayer, mechanically exfoliated MoS_2. For traditional semiconductors such as InN/GaN multiple quantum wells, τ was determined to be ~ 3.34 and 0.10 ps for the E_2 and A_1 modes, respectively [31].

For the vibrational emission spectrum analysis discussed above, we formed our few layer WSe_2 crystallites using solution-based approaches and the inks of this semiconductor were then used to

create heterostructure photodetectors with graphene on flexible polyimide (PI) substrates. Figure 3(a) illustrates the schematic representation of the WSe_2-graphene heterostructure photodetector where the WSe_2 ink was printed on the polyimide film, followed by the graphene ink on top of it (details discussed in the "Methods" Section). Figure 3(b) provides a prototypical demonstration for an array of actual printed photodetectors over large formats (600 μm square WSe_2 layer; graphene traces were 80 μm wide, with a spacing of 125 μm amongst them), where the inset on the right is a magnified view of a single fabricated heterostructure photodetector device. Further material characterization studies were conducted to gauge the surface morphology of the printed structures using scanning electron microscopy (SEM), where the micrographs are shown in Figures 3(c)-(e). For the SEM imaging, the heterostructure devices were printed separately on a bare Si substrate to avoid charging, using identical conditions and printing parameters as for the devices made on the polyimide substrates. It is clear from Figure 3(c), the surface topology is largely uniform for the all inkjet printed heterostructure devices, showing a dense and compact film comprised of the solution-cast platelets. Figure 3(d) reveals a top view of the device that clearly shows the graphene traces, with the top-right inset showing the higher magnification areal image of the junction regions. The high-resolution SEM cross-sectional image of the WSe_2-graphene heterostructure device in Figure 3(e), sectioned orthogonally to the plane of the Si substrate, presents a first-order estimate of the WSe_2 thickness, and the printed graphene layer. From this higher magnification image, the platelet size can be deduced to be well below 1 μm, revealing a high packing density that leads to an enhancement in the inter-platelet connectivity which is important for electrical transport studies discussed next.

2.2 Optoelectronic Transport

After completing the material characterization analysis on the few layer WSe_2 and fabricating the inkjet printed photodetectors, we then proceeded with the electronic and optoelectronic transport measurements on our devices conducted over a range of T from ~ 6 K to 350 K. The device performance of the inkjet printed WSe_2-graphene heterostructure was examined under illumination while the sample was held in vacuum. Figure 4(a) depicts the distinct T-dependent current change observed through the illumination of a broadband light source onto our device, where the LED Driver with Pulse Modulation (Thorlabs DC2200) was used as a light source to control the light intensity irradiated onto the sample. The measured photocurrent I_{ph} increases with increasing T at a fixed light intensity F of 3.2 mW/cm^2. At T ~ 5.5 K, the photocurrent $I_{ph(5.5K)}$ = 1.0 μA, but at high T ~ 350 K, $I_{ph(350K)}$ = 5.3 μA. The bottom-right inset displays the T-dependent I_{ph} at a fixed bias of 40 V that increases as T increases. The top-left inset shows the dark current I_d at room temperature, as a function of voltage. The photoconductivity σ (units of S/m), and linear dynamic range (LDR) data are shown in Figure 4(b), as a function of T at F ~ 3.2 mW/cm^2. Here, σ, defined as the inverse of resistivity ρ, was calculated according to:

$$\sigma = \frac{1}{\rho} \qquad (3)$$

The ρ (in $\Omega \cdot$ m) was extracted from $R = \rho L/A$ equation where A is the cross-sectional area (1.5×10^{-3} cm^2), L is the length of the printed device (~ 600 μm), and R is the resistance at 40 V. The σ increases with T, as is characteristic of a semiconductor. For example, as T increases beyond ~ 125 K, the σ increases due to the temperature-dependent carrier density, where the electrons from the valence band gain sufficient energy to overcome the forbidden region, in order to reach the conduction band.

Every photodetector has a finite range of linear response, which is characterized by the linear dynamic range (LDR), in which the photoresponsivity is constant. The LDR is also indicative of the sensitivity and phase noise of the photodetector which scales according to,

$$LDR = 20\ log\ \frac{I_{ph}}{I_d} \quad (4)$$

Here, I_{ph} is as noted previously, and I_d is the dark current in Amps. At room $T \sim 300$ K, the LDR of the printed WSe_2-graphene photodetector was calculated to be ~ 1.6 dB, and the LDR for prior reported MoS_2 nanomembrane devices appeared to be much larger within the range of ~ 20 dB to 34 dB [27]. Incidentally, in surveying the literature, there appear to be no prior studies that have extracted the LDR for WSe_2-based photodetectors.

Figure 4(c) exhibits the corresponding photoresponsivity R and detectivity D for our devices at $F \sim 3.2$ mW/cm^2 as a function of T at 40 V. The R and D are important figure-of-merit for a photodetector, where the R is calculated using,

$$R = \frac{J_{ph}}{P_{opt}} \quad (5)$$

Here J_{ph} is the photocurrent density (A/cm^2), and P_{opt} is in W/cm^2 and refers to the optical power density. On the other hand, D is tabulated using,

$$D = \frac{A^{1/2}R}{(2qI_d)^{1/2}} \quad (6)$$

where D is measured in cm.Hz$^{1/2}$ W^{-1}(Jones), and A is the effective detector area in cm^2, R is the responsivity, I_d is the dark current in Amps and q is the electron charge = 1.6×10^{-19} C. We see that both R and D are increasing with increasing T particularly significantly beyond 200 K. From Eqn. 5, R was calculated to be ~ 0.7 A/W at room temperature, for our inkjet printed heterostructure device, which is several orders of magnitude higher compared to other reports of printed heterostructures where MoS_2 and WS_2 inks were used [32][33]. Similarly, the D was calculated to be ~ 2.9×10^{10} Jones, which was comparable to previous reports of ~ 3.6×10^{10} Jones [17][34].

Figure 4(d) displays the σ and R as a function of light intensity F at 40 V where F ranged from ~ 0.6 mW/cm^2 to 3.2 mW/cm^2 for our flexible photodetector device. The σ increases considerably from its dark value of ~ 1.9×10^{-1} S/m when $F = 0$, which is significantly higher than previously reported dark current for solution-processed inkjet printed MoS_2 films ($\sigma \sim 2.5 \times 10^{-6}$ S/m) [35]. Under light illumination at $F \sim 3.2$ mW/cm^2, the photoconductivity here reaches ~ 2.3×10^{-1} S/m. From the data in Figure 4(d), R also decreases with increasing F from a value of ~ 2.3 A/W at ~ 0.6 mW/cm^2 to ~ 0.7 A/W at ~ 3.2 mW/cm^2.

Figure 5(a) displays the I_{ph} as a function of T for various wavelengths ranging from 400 nm to 900 nm. As T increases, I_{ph} also increases, as expected for a semiconductor, although the converse is evident with increasing wavelength, where I_{ph} decreases; this is seen more clearly from the data in the inset of Figure 5(a). From this analysis, it is understandable that the photodetector absorbs more photons within the visible region (400 - 700 nm) and is still operational in the near IR region. Figure 5(b) shows the temporal response of the I_{ph} at a constant bias of 40 V, illuminated with $F \sim$ 0.6, 1.9, and 3.2 mW/cm^2 using our broadband white light source. A fast I_{ph} increase was observed for all three F thresholds, with a subsequent slow increase; this behavior is similar for the decaying edge, which first shows a fast decay, and subsequently, a slow decay path is then observed. Usually, such a slow rise and decay region of the photocurrent response are convincing signs of the presence of traps [35], which has been analyzed in prior studies on few layer (or monolayer) 2D MoS_2 [36][37]. Similarly, the fast I_{ph} rise and decay has been witnessed previously for 2D materials by a number of groups [38][39]. Figure 5(c) illustrates the ratio of the I_{Light}/I_{Dark} response with respect to F, where I_{Light} is the current under illumination and I_{Dark} is the current in the dark (such that $I_{ph} = I_{Light} - I_{Dark}$). The response increases almost linearly with increasing illumination F

~ 0.6 mW/cm^2, 1.3 mW/cm^2, 1.9 mW/cm^2, 2.6 mW/cm^2, to 3.2 mW/cm^2 reaching ~ 1.56 at ~ 3.2 mW/cm^2.

From the temporal analysis, the time constants associated with the rising and falling edges are defined as τ_{rise} and τ_{decay}, respectively, for the photocurrent which is plotted as a function of F in Figure 5(d). Here, we see that the time constants are fairly invariant with F, though there is some mild decrease in the rising edges as F increases. At ~ 0.6 mW/cm^2, the τ_{rise} and τ_{decay} were found to be ~ 102.8 ms and 100.7 ms, respectively, while at ~ 3.2 mW/cm^2, the τ_{rise} and τ_{decay} were found to be lower, ~ 100.9 ms and 99.9 ms, respectively. The reported values of τ_{rise} and τ_{decay} were significantly lower compared to prior studies conducted on MoS_2 films [40], where τ_{rise} ~ 80 s and τ_{decay} ~ 30 s at F ~ 10 mW/cm^2. Higher τ_{rise} and τ_{decay} normally are signs of trapping within the printed WSe_2 film, which is mainly due to the disordered nature of the nano-platelet arrays which exhibit defects including from edge states that serve as energetically favorable recombination sites.

2.3 Strain-dependent Optoelectronic and Atomic Vibrational Properties

Strain-dependent mechanical bending tests were performed on our devices to validate the mechanical durability of the printed flexible photodetector. The 3D printed fixtures with five radii of curvatures υ were used for these bending tests, which ranged in value from 0.072 cm^{-1}, 0.087 cm^{-1}, 0.112 cm^{-1}, 0.157 cm^{-1}, 0.262 cm^{-1}. Using this fixture, the I_{ph} and R were measured as a function of strain and under varying light intensity. The flexible heterostructure device was attached to the 3D fixture as shown in the top inset of Figure 6(a), in this case for υ ~ 0.262 cm^{-1}. A double-sided tape was used for mounting the sample onto the fixture. Figure 6(a) shows the I_{ph} as a function of F for υ ~ 0.112 cm^{-1}, ~ 0.157 cm^{-1} and ~ 0.262 cm^{-1}. The I_{ph} decreased with increasing υ, and with higher F, the I_{ph} increases for each bending. The possible explanation for

this behavior with increasing strain has likely to do with the membrane-to-membrane separation increasing, that causes a drop in I_{ph}; this is consistent with prior reports that have explored strain-dependent properties of the electronic transport in other material systems [41]. Figure 6(b) depicts the dependence of I_{ph} and R (where $R = \frac{J_{ph}}{P_{opt}}$) as a function of υ, captured at a F of ~ 3.2 mW/cm^2, where both parameters decrease with more bending. On a flat surface (υ = 0 cm^{-1}), the photodetector generated the highest I_{ph} where maximal charge separation and collection occurs at the graphene electrodes, while increasing curvature reduced the I_{ph}. The strain causes mechanical deformation and produces piezoelectric charges at the heterostructure interface. The electric field at the interface and the increased metal-semiconductor junction provides a smaller driving force to separate photo-generated electron-hole pairs, which reduces I_{ph}. Figure 6(c) displays four repetitive cycles of I_{ph} as a function of F for υ ~ 0.262 cm^{-1}. In the first cycle, F ranged from ~ 0.6 to 3.2 mW/cm^2 with a time delay of 10 seconds during each measurement. As seen in Figure 6(c), the I_{ph} did not change significantly for all the four cycles and showed a similar trend with F, which ensures good reproducibility of photocarrier generation and collection in our printed photodetector devices.

In addition to strain-dependent measurements conducted on the photodetector devices itself, we also initiated mechanical strain-dependent measurements *in-situ* using Raman spectroscopy at the same υ that were used for the photodetector measurements. The printed WSe_2 on the PI substrate was mounted on the 3D printed fixtures and Figure 6(d) displays the schematic of our experimental set-up for the strain-dependent Raman measurements conducted on the flexible, printed WSe_2 film at λ = 532 nm while applying mechanical strain. The inset in Figure 6(d) displays the E^1_{2g} and A_{1g} vibrational modes which were reflected in the ensuing Raman shifts we observed for the vibrational modes of WSe_2 as strain increased. Figure 6(e) illustrates the nonlinear blue-

shift for both the E^1_{2g} and A_{1g} peaks under strain compared to when the sample was placed on a flat surface; here a blue-shift of ~ 1.73 cm^{-1} was observed for the E^1_{2g} peak position which is about twice that of the A_{1g} peak (~ 0.87 cm^{-1}). This blue-shift maybe attributed to bond stretching resulting from a macroscopic deformation [42]. However, phonon interactions with localized defects, nature of the stacking, and the substrate used can also be influential factors which would be interesting areas for further study in a future work. Figure 6(f) displays the change in the E^1_{2g} and A_{1g} peak intensities with respect to υ and interestingly, the intensity of both peaks increases with increasing curvature. The increased intensity of the E^1_{2g} and A_{1g} peak with strain is explained on the basis of the increase in radiative recombination events present due to possible bond stretching [43], but the determination of the exact mechanism will require further experimentation in a future study.

2.4 Capacitance-Frequency Response

Understanding the nature of deep traps is important as they affect several optoelectronic properties relevant to achieving high-performance devices. For example, trap states introduce recombination centers and charged point sites. The WSe_2-graphene heterostructure was probed in the cryogenic probe stage used previously, and capacitance C-frequency f measurements were made as in prior work [44][45] [46], as a function of temperature T to comment on the nature of the deep trap states. In this technique, as the frequency decreases, deeper traps participate and contributes to the capacitance, and hence, capacitance increases as seen in Figure 7, where the f was varied from ~ 10 kHz to 500 kHz. The junction-capacitance also increased at higher temperatures over the entire f range tested. As the f is swept from high to low values, trap states located deeper into the bandgap respond to the signal. Further characterization and analysis would be required to decipher the dependence of the trap emission rate as a function of temperature to determine the trap-state

densities and their energies.

3. Summary and Conclusions

In this paper, we have experimentally studied the *T*-dependent Raman spectra of liquid exfoliated few layer WSe_2 from ~ 80 K to 573 K, while at the same time the *T*-dependent optoelectronic characterization of our all inkjet printed WSe_2-graphene heterostructure photodetector was also measured. Increasing *T* caused phonon shifts, described by the first-order *T* coefficients for the E^1_{2g} and A_{1g} modes, $\chi_{E^1_{2g}}$, $\chi_{A_{1g}}$ which were calculated to be - 0.018 cm^{-1}/k. The phonon lifetime τ was computed to be ~ 0.57 and 0.74 ps for the E^1_{2g}, A_{1g} modes, respectively, at room *T*. The SEM reveals a high packing density within our heterostructure films that leads to an enhancement in the inter-platelet connectivity of the 2D materials. The printed photodetector demonstrated conductivity $\sigma \sim 2.3 \times 10^{-1}$ S/m, which implies a significant improvement compared to prior reports. The photodetector figures of merit *R* and *D* were determined to be ~ 0.7 A/W and ~ 2.9×10^{10} Jones, respectively. From the rise and decay of the I_{ph} with respect to *F*, the τ_{rise} and τ_{decay} were found to be ~ 100.9 ms and 99.9 ms, respectively. Strain-dependent measurements were also conducted that showed the I_{ph} with strain levels for $\upsilon \sim 0.262$ cm^{-1}, indicating the feasibility of such devices for large format arrays printed on flexible substrates. Lastly, *C-f* measurements were performed as a function of *T*, which showed the capacitance to increase as temperature increased up to 500 kHz. As shown in this work, our promising results are a stepping stone for the use of WSe_2 absorbers and its hybridization with other materials to boost the performance and photodynamics of photodetectors on bendable substrates.

4. Experimental Methods

Process to Formulate Inks and Inkjet Printing

Both the graphene and WSe_2 inks were formulated using ultrasonic bath sonication of the graphene/WSe_2 powder in C/T (a mixture of Cyclohexanone/Terpineol (C/T) at a ratio of 7:3). Surfactant Ethyl Cellulose (EC) (2.5 wt%) and graphene/WSe_2 powder (graphene - 15 mg/ml; WSe_2 - 35 mg/ml) were then added, respectively, in 10 ml of C/T and sonicated for 24 hours. After 24 hours, the inks were centrifuged for 10 minutes at 1,000 rpm to sediment the thick membranes. The supernatant in a volume of ~ 9 ml was collected and another 5 mg/ml of graphene/WSe_2 was added to the solution to increase the density of the dispersion and ensure a sufficient amount of graphene/WSe_2 membranes are present in the ink. This was followed by another 24 hours of ultra-sonication. Then, the top 8 ml supernatant was taken out and transferred to the cartridge of the Dimatix Materials Printer (DMP-2831 Series) for inkjet printing the devices.

Preparing WSe_2 Sample for Raman Temperature Study

For the Raman and ensuing temperature-dependent measurements, 0.5 ml of the WSe_2 ink was extracted and dispersed onto an SiO_2/Si substrate using spin coating. The Laurell spin coater (WS-650-23NPP) was used to spin coat the ink at 1000 rpm for 20 sec. This procedure was used so as to increase the likelihood of isolating single/few layer WSe_2 membranes, since inkjet printing can result in stacking up of multiple membranes during printing, which minimizes the chance of obtaining thinner membranes.

Photodetector Device Fabrication

To achieve higher inkjet printing resolution, four nozzles were used for printing the material and device structures compared to the case where all 16 nozzles were used; the latter often resulted in non-uniform line edges due to ink spreading on the substrate [18][47][48]. The heterostructure device with graphene traces (electrode) and a photoactive WSe_2 layer were printed on a flexible PI film. First, a 600 μm square WSe_2 layer was printed with 15 ink passes and then annealed at an

ambient environment on a hotplate at 330°C for 3 hours using the approach described in the "Sample Annealing" portion within this Methods Section. Then, the printed PI film was placed back at the same (x,y) coordinates to print the next 8 ink passes of the graphene layer and then annealed at ambient atmosphere on a hotplate at 330°C for 3 hours using the same technique. The graphene traces were 80 μm wide, with a spacing of 125 μm amongst them. Identical conditions were used to print and anneal the graphene traces. The printed WSe_2 thickness was found to be ~ 0.9 μm after all the annealing steps were completed.

Sample Annealing

The temperature was ramped at a rate of ~ 2.2°C/minute from 70°C to 330°C. The duration of the entire process was 3 hours to completely anneal our samples. For printed graphene and WSe_2, two separate annealing steps were taken. After the standard ambient annealing step, an additional annealing step was conducted with the rotary evaporator. This showed the thickness to decrease significantly after another 5 hours of annealing. There were entrapped solvents present even after ambient annealing, which the rotary evaporator was effective in further removing.

Disclosures

The authors declare no conflicts of interests.

Acknowledgments

We greatly appreciate the support received from the Air Force Office of Scientific Research (grant number FA9550-15-1-0200 and FA9550-21-1-0404) and the Office of Naval Research (grant

number ONR N00014-20-1-2597) that enabled us to pursue this work. A.B.K. is also grateful to the support received from the PACCAR Endowed Professorship.

REFERENCES:

[1] X. Liu *et al.*, "Strong light–matter coupling in two-dimensional atomic crystals," *Nat. Photonics* **9**, 30 (2015).
[2] L. Britnell *et al.*, "Strong light-matter interactions in heterostructures of atomically thin films," *Science* **340**, 1311 (2013).
[3] K. F. Mak and J. Shan, "Photonics and optoelectronics of 2D semiconductor transition metal dichalcogenides," *Nat. Photonics* **10**, 216 (2016).
[4] K. S. Novoselov *et al.*, "Two-dimensional atomic crystals," *Proc. Natl. Acad. Sci.* **102**, 10451 (2005).
[5] K. F. Mak, C. Lee, J. Hone, J. Shan, and T. F. Heinz, "Atomically thin MoS 2: a new direct-gap semiconductor," *Phys. Rev. Lett.* **105**, 136805 (2010).
[6] D. Xiao, G.-B. Liu, W. Feng, X. Xu, and W. Yao, "Coupled spin and valley physics in monolayers of MoS 2 and other group-VI dichalcogenides," *Phys. Rev. Lett.***108**, 196802 (2012).
[7] Z. Yin *et al.*, "Single-layer MoS2 phototransistors," *ACS Nano* **6**, 74 (2012).
[8] S. Xu *et al.*, "Odd-integer quantum Hall states and giant spin susceptibility in p-type few-layer WSe 2," *Phys. Rev. Lett.* **118**, 67702 (2017).
[9] E. Courtade *et al.*, "Charged excitons in monolayer WSe 2: experiment and theory," *Phys. Rev. B* **96**, 85302 (2017).

[10] H. Fang, S. Chuang, T. C. Chang, K. Takei, T. Takahashi, and A. Javey, "High-performance single layered WSe2 p-FETs with chemically doped contacts," *Nano Lett.***12**, 3788 (2012).
[11] Q. Cheng *et al.*, "WSe2 2D p-type semiconductor-based electronic devices for information technology: Design, preparation, and applications," *InfoMat*. **2**, 656 (2020).
[12] W. Zhao *et al.*, "Evolution of electronic structure in atomically thin sheets of WS2 and WSe2," *ACS Nano* **7**, 791 (2013).
[13] Z. Y. Zhu, Y. C. Cheng, and U. Schwingenschlögl, "Giant spin-orbit-induced spin splitting in two-dimensional transition-metal dichalcogenide semiconductors," *Phys. Rev. B* **84**, 153402 (2011).
[14] A. S. Bandyopadhyay, N. Adhikari, and A. B. Kaul, "Quantum Multi-body Interactions in Halide-assisted Vapor Synthesized Monolayer WSe2 and Its Integration in a High Responsivity Photodiode with Low Interface Trap Density," *Chemistry of Materials* **31**, 9861 (2019).
[15] D. J. Late, S. N. Shirodkar, U. V Waghmare, V. P. Dravid, and C. N. R. Rao, "Thermal Expansion, Anharmonicity and Temperature-Dependent Raman Spectra of Single-and Few-Layer MoSe2 and WSe2," *ChemPhysChem*. **15**, 1592 (2014).
[16] C. Buga and J. C. Viana, "Inkjet printing of functional inks for smart products," in *Production Engineering and Robust Control*, IntechOpen, 2022.
[17] R. F. Hossain, I. G. Deaguero, T. Boland, and A. B. Kaul, "Biocompatible, large-format, inkjet printed heterostructure MoS 2-graphene photodetectors on conformable substrates," *npj 2D Mater. Appl.* **1**, 1 (2017).
[18] M. Michel *et al.*, "A thermally-invariant, additively manufactured, high-power graphene resistor for flexible electronics," *2D Mater.* **4**, 25076 (2017).
[19] R. F. Hossain and A. B. Kaul, "Inkjet-printed MoS2-based field-effect transistors with graphene and hexagonal boron nitride inks," *J. Vac. Sci. Technol. B* **38**, 42206, (2020).
[20] C. Casiraghi, M. Macucci, K. Parvez, R. Worsley, Y. Shin, F. Bronte, C. Borri, M. Paggi, and G. Fiori, "Inkjet printed 2D-crystal based strain gauges on paper," *Carbon* **129**, 462 (2018).
[21] S. Kim *et al.*, "Inkjet-printed antennas, sensors and circuits on paper substrate," *IET Microwaves, Antennas Propag.* **7**, 858 (2013).
[22] A. G. Kelly *et al.*, "All-printed thin-film transistors from networks of liquid-exfoliated nanosheets," *Science* **356**, 69 (2017).
[23] A. B. Patel *et al.*, "Electrophoretically deposited MoSe2/WSe2 heterojunction from ultrasonically exfoliated nanocrystals for enhanced electrochemical photoresponse," *ACS Appl. Mater. Interfaces* **11**, 4093 (2019).
[24] P. Tonndorf *et al.*, "Photoluminescence emission and Raman response of monolayer MoS 2, MoSe2, and WSe2," *Opt. Express* **21**, 4908 (2013).
[25] H. Zeng *et al.*, "Optical signature of symmetry variations and spin-valley coupling in atomically thin tungsten dichalcogenides," *Sci. Rep.* **3**, 1608 (2013).
[26] I. Calizo, A. A. Balandin, W. Bao, F. Miao, and C. N. Lau, "Temperature dependence of the Raman spectra of graphene and graphene multilayers," *Nano Lett.* **7**, 2645 (2007).
[27] M. F. Khan, G. Nazir, V. M. Lermolenko, and J. Eom, "Electrical and photo-electrical properties of MoS2 nanosheets with and without an Al2O3 capping layer under various environmental conditions," *Sci. Technol. Adv. Mater.* **17**, 166 (2016).
[28] F. Wagle, G. Steinle-Neumann, and N. de Koker, "Saturation and negative temperature

coefficient of electrical resistivity in liquid iron-sulfur alloys at high densities from first-principles calculations," *Phys. Rev. B* **97**, 94307 (2018).
[29] N. A. Lanzillo *et al.*, "Temperature-dependent phonon shifts in monolayer MoS2," *Appl. Phys. Lett.* **103**, 93102 (2013).
[30] P. J. Ko, A. Abderrahmane, T. V. Thu, D. Ortega, T. Takamura, and A. Sandhu, "Laser power dependent optical properties of mono-and few-layer MoS2," *J. Nanosci. Nanotechnol.***15**, 6843 (2015).
[31] H. Xia *et al.*, "Numerical calculation of optical phonon decay rate in InN/GaN MQW," *IOP Conference Series: Materials Science and Engineering* **68**, 12009 (2014).
[32] F. Withers *et al.*, "Heterostructures produced from nanosheet-based inks," *Nano Lett.* **14**, 3987 (2014).
[33] J. Li, M. M. Naiini, S. Vaziri, M. C. Lemme, and M. Östling, "Inkjet printing of MoS2," *Adv. Funct. Mater.* **24**, 6524 (2014).
[34] S. Mukherjee, R. Maiti, A. K. Katiyar, S. Das, and S. K. Ray, "Novel colloidal MoS2 quantum dot heterojunctions on silicon platforms for multifunctional optoelectronic devices," *Sci. Rep.* **6**, 29016 (2016).
[35] D. J. Finn *et al.*, "Inkjet deposition of liquid-exfoliated graphene and MoS 2 nanosheets for printed device applications," *J. Mater. Chem. C* **2**, 925 (2014).
[36] O. Lopez-Sanchez, D. Lembke, M. Kayci, A. Radenovic, and A. Kis, "Ultrasensitive photodetectors based on monolayer MoS2," *Nat. Nanotechnol.* **8**, 497 (2013).
[37] W. Zhang, J. Huang, C. Chen, Y. Chang, Y. Cheng, and L. Li, "High-gain phototransistors based on a CVD MoS2 monolayer," *Adv. Mater.* **25**, 3456 (2013).
[38] W. Choi *et al.*, "High-detectivity multilayer MoS2 phototransistors with spectral response from ultraviolet to infrared," *Adv. Mater.***24**, 5832 (2012).
[39] Z. Zeng *et al.*, "An effective method for the fabrication of few-layer-thick inorganic nanosheets," *Angew. Chemie Int. Ed.* **51**, 9052 (2012).
[40] G. Cunningham *et al.*, "Photoconductivity of solution-processed MoS 2 films," *J. Mater. Chem. C* **1**, 6899 (2013).
[41] T. Sekine, K. Fukuda, D. Kumaki, and S. Tokito, "The effect of mechanical strain on contact resistance in flexible printed organic thin-film transistors," *Flex. Print. Electron.* **1**, 35005 (2016).
[42] R. J. Day, V. Piddock, R. Taylor, R. J. Young, and M. Zakikhani, "The distribution of graphitic microcrystals and the sensitivity of their Raman bands to strain in SiC fibers," *J. Mater. Sci..***24**, 2898 (1989).
[43] Y. He *et al.*, "Strain-induced electronic structure changes in stacked van der Waals heterostructures," *Nano Lett.* **16**, 3314 (2016).
[44] J. A. Carr and S. Chaudhary, "On the identification of deeper defect levels in organic photovoltaic devices," *J. Appl. Phys.* **114**, 64509 (2013).
[45] J. Bhattacharya, R. W. Mayer, M. Samiee, and V. L. Dalal, "Photo-induced changes in fundamental properties of organic solar cells," *Appl. Phys. Lett.* **100**, 193501 (2012).
[46] T. Walter, R. Herberholz, C. Müller, and H. W. Schock, "Determination of defect distributions from admittance measurements and application to Cu (In, Ga)Se2 based heterojunctions," *J. Appl. Phys.* **80**, 4411 (1996).
[47] R. F. Hossain, M. Min, L.-C. Ma, S. R. Sakri, and A. B. Kaul, "Carrier photodynamics in 2D perovskites with solution-processed silver and graphene contacts for bendable optoelectronics," *npj 2D Mater. Appl.* **5**, 1 (2021).

[48] M. Min, R. F. Hossain, N. Adhikari, and A. B. Kaul, "Inkjet-Printed Organohalide 2D Layered Perovskites for High-Speed Photodetectors on Flexible Polyimide Substrates," *ACS Appl. Mater. Interfaces* **12**, 10809 (2020).

List of Figures

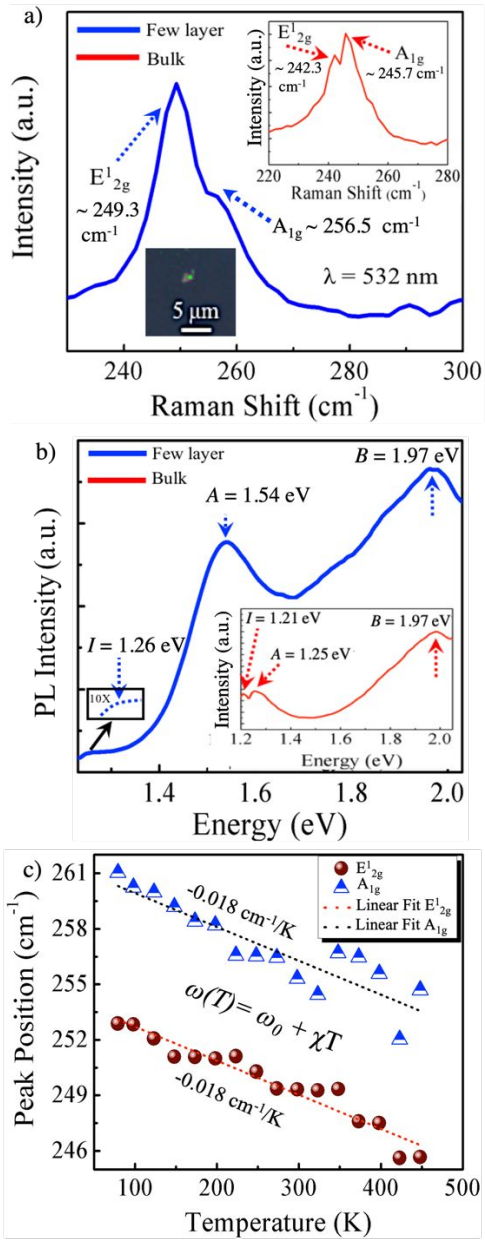

Figure 1: (a) Raman spectra of few layer WSe_2 using Raman excitation wavelength λ = 532. The spectra show the E^1_{2g} and A^1_g peaks appearing at ~ 249.3 cm^{-1} and ~ 256.5 cm^{-1}, respectively. The intensity of the A^1_g peak was almost half that of the E^1_{2g} peak, which suggests that the exfoliated WSe_2 flakes are few layer. The bottom left inset displays the WSe_2 flake that was isolated for the Raman measurements, by spin coating the WSe_2 ink on the SiO_2/Si substrate. The top right inset is the Raman spectra for bulk WSe_2, where the intensity of the A^1_g peak is significantly higher. (b) The PL spectra of few layer WSe_2 at room temperature shows the excitonic emission bands centered at A ~ 1.54 eV and B ~ 1.97 eV, respectively, with an indirect I peak at ~ 1.26 eV shown on the magnified bottom left inset; the bottom right inset depicts the PL of bulk WSe_2 where both

the *A* and *I* peaks are red-shifted, as compared to the few-layer case. c) The temperature-dependent E^1_{2g} and A_{1g} peak positions, where the linear fit yields $\chi_{E^1_{2g}}$, $\chi_{A_{1g}}$~ - 0.018 cm^{-1}/K. These values are summarized in Table I and compared to other materials.

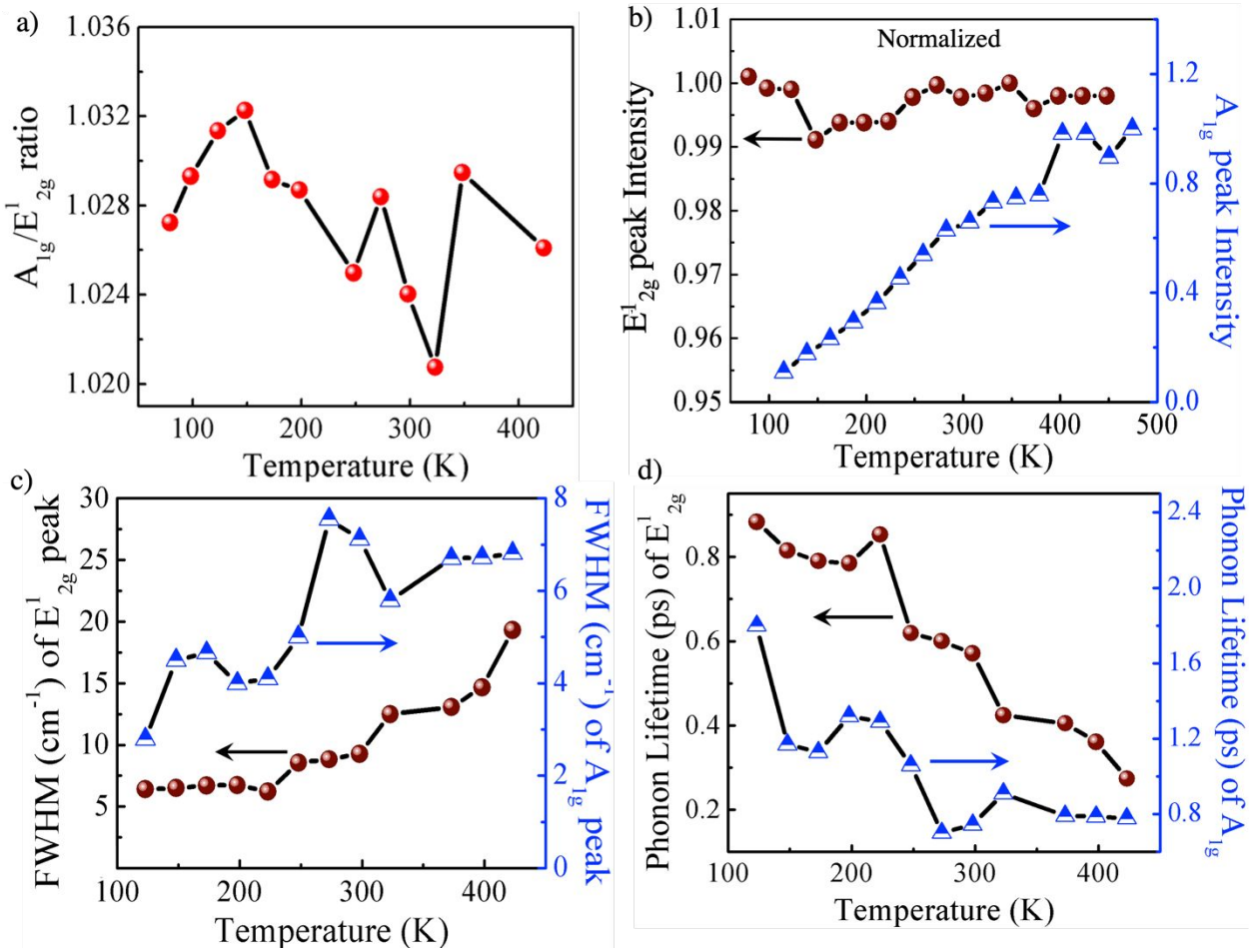

Figure 2: a) The A_{1g}/E^1_{2g} intensity ratio as a function of temperature, which shows above ~ 150 K, the ratio is largely decreasing. (b) The change in normalized E^1_{2g} and A_{1g} peak intensities with temperature, where the data corresponding to the E^1_{2g} peak appears temperature invariant. c) Measured values of the FWHM, Γ from ~ 80 K to ~ 450 K. d) Variation in the phonon lifetime τ derived from Γ for the Raman-active E^1_{2g} and A_{1g} modes, indicating τ decreases with increasing temperature, as expected due to dissipation from a more active phonon spectrum at higher temperatures.

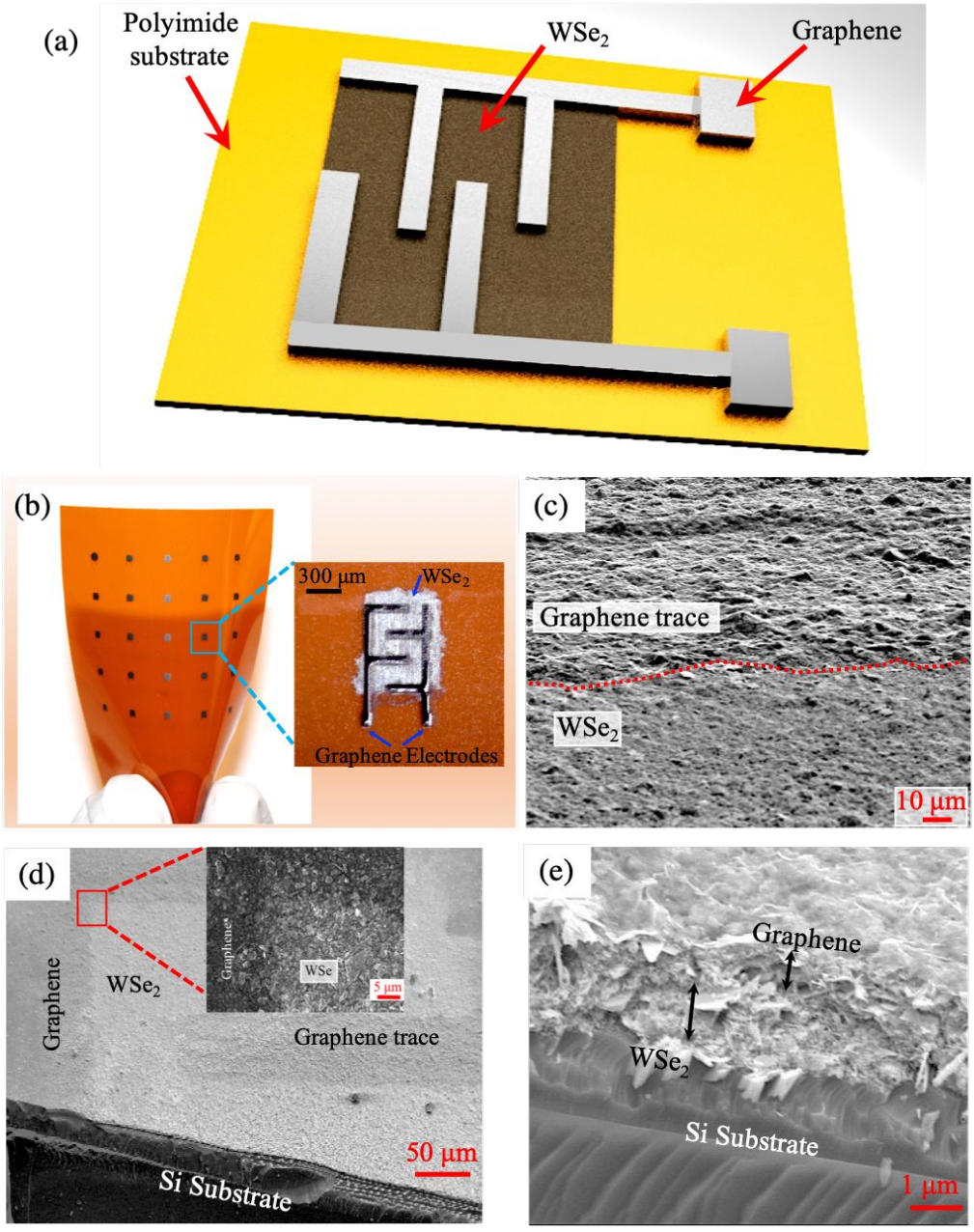

Figure 3: (a) Schematic diagram of the flexible WSe_2-graphene heterostructure device used for the temperature-dependent optoelectronic characterization studies. (b) An array of all inkjet printed hetero-structure devices printed on flexible PI substrates over an area of ~ 6 cm x 5 cm. The inset shown on the right is the image of a single inkjet printed photodetector, where graphene electrodes were printed on top of the WSe_2 layer. (c) SEM image showing the morphology of the semiconducting WSe_2 and graphene to be uniform and dense for our printed devices. (d) the lower magnification SEM of the device shows a well-defined graphene trace visible over the underlying WSe_2 film with the higher magnification of the junction region depicted in the inset. (e) Cross-

sectional SEM view of the WSe_2-graphene layer on a Si substrate, which allowed us to decipher the thickness to some extent, and confirms the average size of the platelets is well below ~ 1 μm.

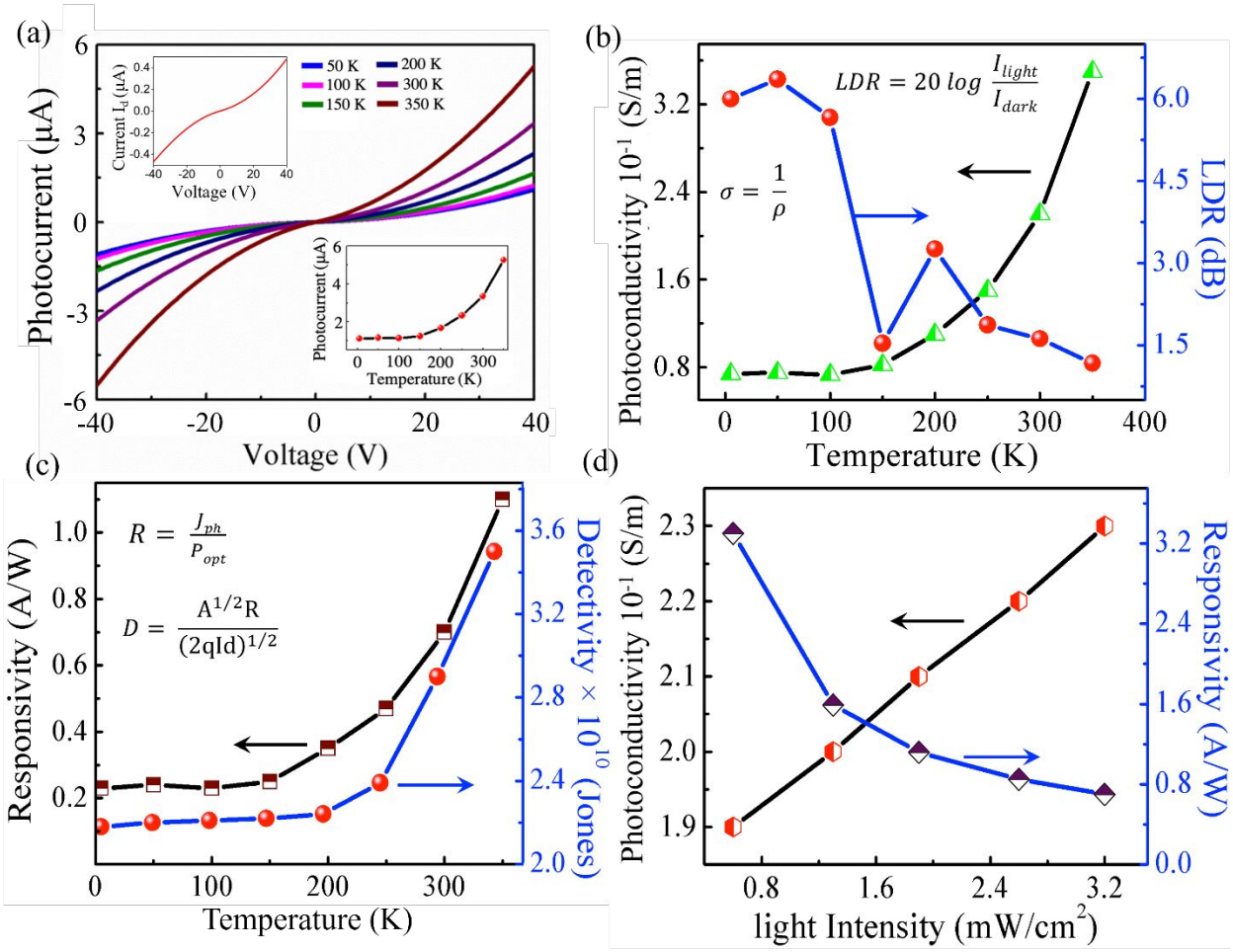

Figure 4: a) The I-V Characteristic measured from ~ 50 K to ~ 350 K, where the photocurrent I_{ph} is seen to increase with temperature. Inset at the bottom-right displays the T-dependent I_{ph} at 40 V using a broadband excitation light source in vacuum. The I_d-V characteristic is shown in the dark ($F = 0$) at room temperature within the top-left inset. b) The conductivity σ and linear dynamic range (LDR) as a function of temperature, which indicates that σ increases steeply while the LDR decreases nonlinearly with increasing T. c) The responsivity R and detectivity D as a function of T at 40 V (for light intensity $F \sim 3.2$ mW/cm^2); here the R and D were calculated to be ~ 0.7 A/W and 2.9 x 10^{10} Jones, respectively, at room temperature. d) The σ and R as a function of F, where σ increases linearly and R appears to decrease with increasing F.

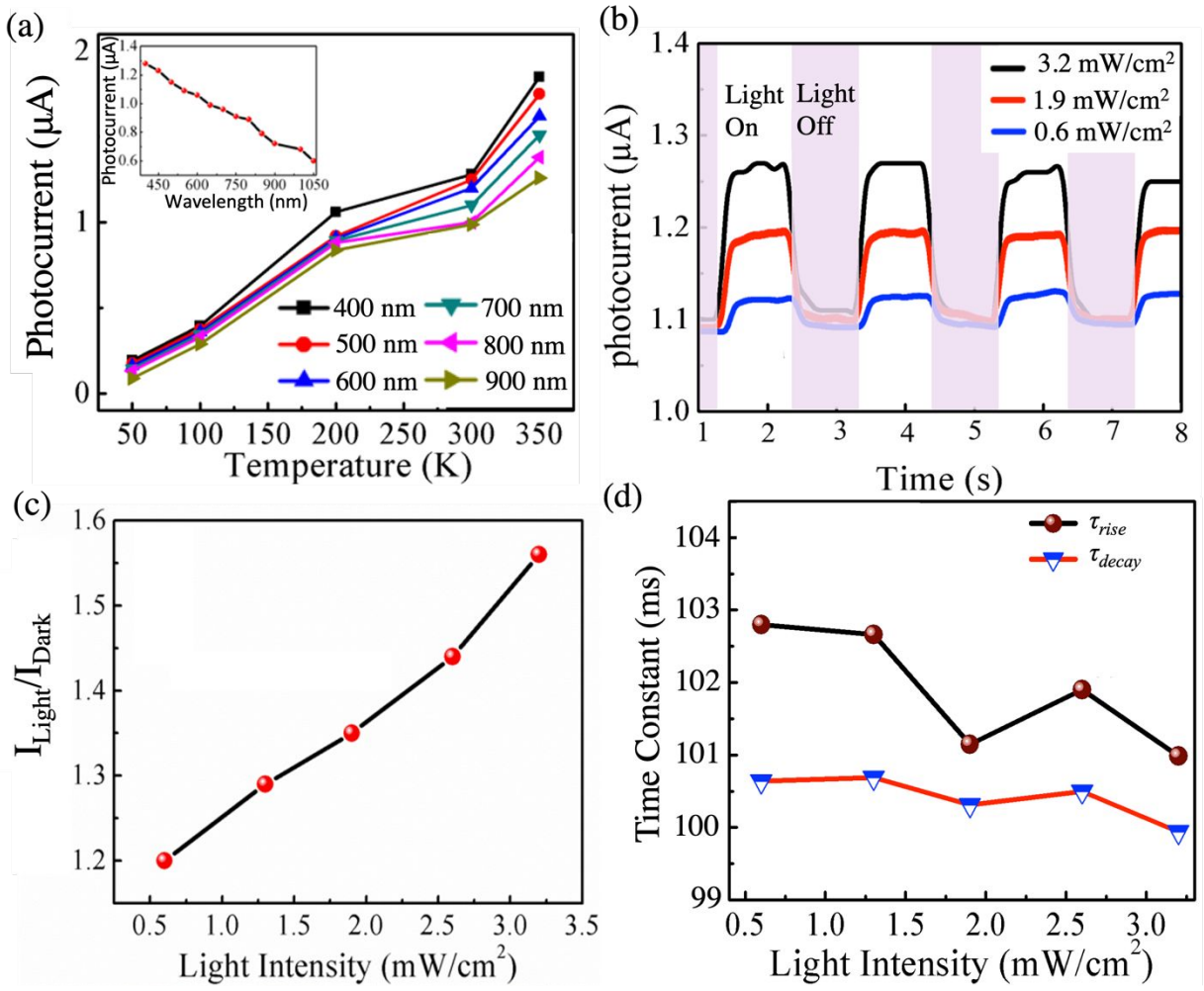

Figure 5: (a) Wavelength-dependent I_{ph} as a function of temperature for our inkjet printed flexible heterostructure, where measurements were made from ~ 400 nm to 1100 nm in the visible to the infrared regime, respectively, and with a bias voltage of ~ 40 V applied in vacuum. Inset shows I_{ph} with wavelengths at room temperature. (b) Periods of ON/OFF light pulses allowed for the tabulation of the temporal response of the I_{ph} for three different F (~ 0.8, 1.9 and 3.2 mW/cm^2) at a 40 V bias. (c) Normalized I_{Light}/I_{Dark} response with F ranging from ~ 0.6 mW/cm^2 to 3.2 mW/cm^2. (d) Time constants τ_{rise} and τ_{decay} of I_{ph} plotted as a function of F; at ~ 0.6 mW/cm^2, the τ_{rise} and τ_{decay} were ~ 102.8 ms and 100.7 ms, respectively, while at ~ 3.2 mW/cm^2, they were slightly lower, ~ 100.9 ms and 99.9 ms, respectively.

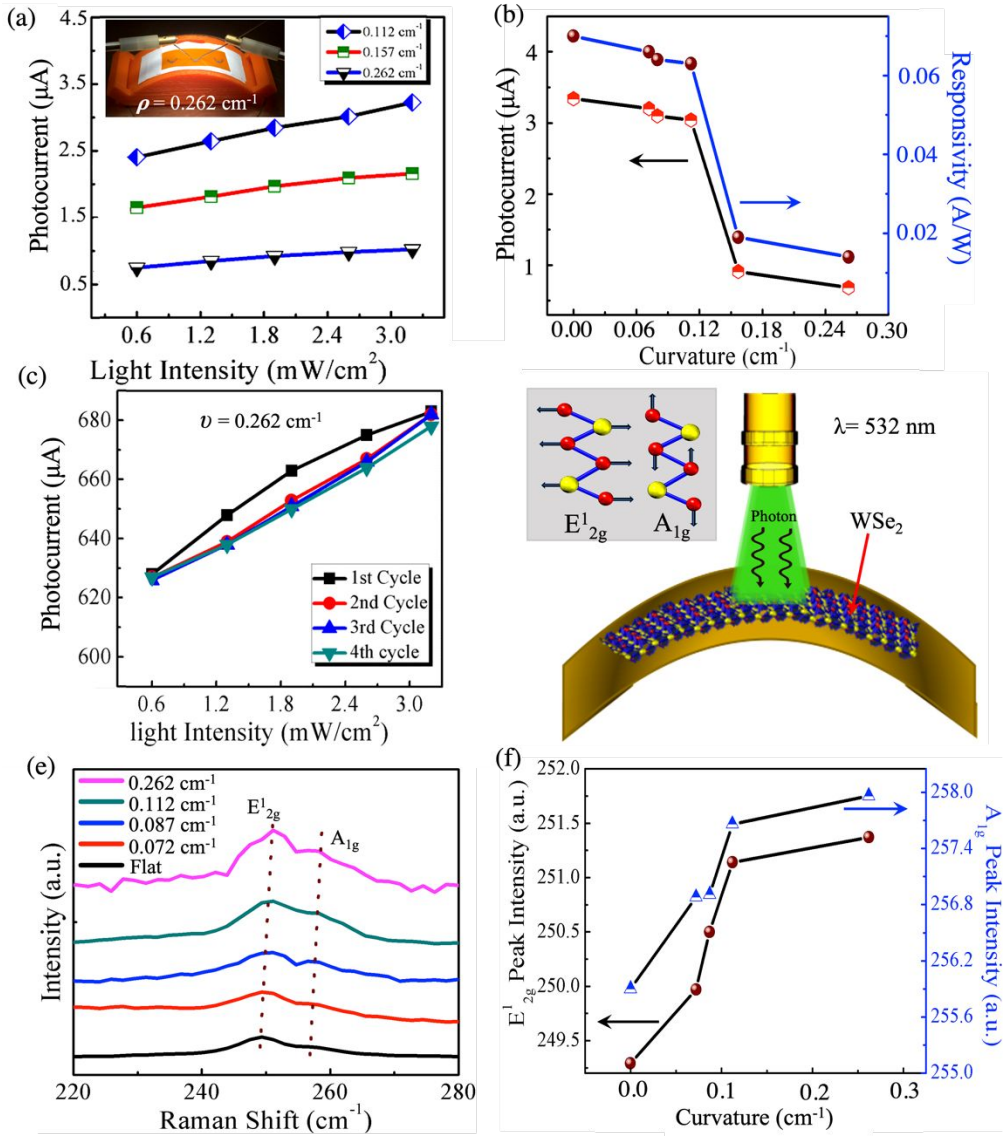

Figure 6: (a) The relative I_{ph} change as a function of F at strain levels represented by the following radii of curvature: $\upsilon \sim$ (i) 0.112 cm^{-1}, (ii) 0.157 cm^{-1}, (iii) 0.262 cm^{-1}. The inset depicts an example of the 3D printed fixture used upon which the device was mounted for these strain-dependent measurements. (b) The I_{ph} and R as a function of curvature to gauge the effect of strain at $F \sim 3.2$ mW/cm^2 where both parameters appear to decrease with bending. (c) Four repetitive cycles of the I_{ph} measured under various F at $\upsilon \sim 0.262$ cm^{-1} suggests good reproducibility of the photocarrier generation within the device. (d) Schematic representation of the printed WSe_2 on a polyimide (PI) substrate, optically excited using a wavelength $\lambda = 532$ nm within the Raman system for the strain-dependent Raman measurements. The inset displays the Raman active in-plane E^1_{2g} and out-of-plane A_{1g} vibrational modes. e) The blue-shift observed in both the E^1_{2g} and A_{1g} peaks under strain at the various radii of curvature used. (f) The change in intensities of the E^1_{2g} and A_{1g} peaks with υ shows that the intensities in both of the modes are increasing with strain.

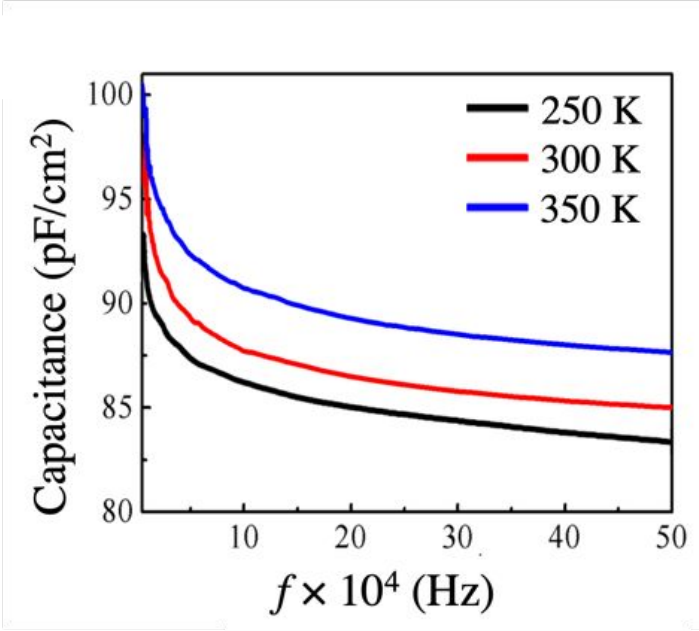

Figure 7: The capacitance *C* as a function of frequency *f* for temperatures ~ 250 K, 300 K, and 350 K used in these experiments. The highest *C* was determined to be at ~ 350 K and the *C* increased with *T* across the entire frequency sweep from ~ 10 kHz up to 500 kHz.

List of Tables

TABLE I. Comparison of $\chi_{E^1_{2g}}$ and $\chi_{A_{1g}}$ for liquid exfoliated WSe_2 with that of MoS_2 (units of cm^{-1}/K).

	$\chi_{E^1_{2g}}$ (cm^{-1}/K)	$\chi_{A_{1g}}$ (cm^{-1}/K)	Reference
Few layer WSe_2, liquid exfoliation	**- 0.018**	**- 0.018**	**This work**
Few layer MoS_2, liquid exfoliation	- 0.014	- 0.016	[27]

TABLE II. Comparison of phonon lifetime for few layer WSe_2 at room T with other reported materials (units of ps).

Material System	Raman Modes	Phonon Lifetime (ps)	Reference
Few layer WSe_2, liquid exfoliated	E^1_{2g}, A_{1g}	**0.57, 0.74**	**This work**
Few layer MoS_2, liquid exfoliated	E^1_{2g}, A_{1g}	2.2, 1.8	[27]
Monolayer MoS_2, mechanically exfoliated	E^1_{2g}, A_{1g}	1.8, 0.84	[30]
InN/GaN (multiple quantum wells)	E_2, A_1	3.34, 0.10	[31]